

Hydrodynamical Non-radiative Accretion Flows in Two-Dimensions

James M. Stone¹ James E. Pringle¹

¹Institute of Astronomy, Cambridge University, Madingley Road, Cambridge CB3 0HA, UK

²Department of Astronomy, University of Maryland, College Park, MD 20742 USA

and

Mitchell C. Begelman^{1,2,3}

³JILA, University of Colorado, Boulder, CO 80309-0440 USA

⁴ITP, University of California, Santa Barbara, CA 93106-4030 USA

Received _____; accepted _____

ABSTRACT

Two-dimensional (axially symmetric) numerical hydrodynamical calculations of accretion flows which cannot cool through emission of radiation are presented. The calculations begin from an equilibrium configuration consisting of a thick torus with constant specific angular momentum. Accretion is induced by the addition of a small anomalous azimuthal shear stress which is characterized by a function ν . We study the flows generated as the amplitude and form of ν are varied. A spherical polar grid which spans more than two orders of magnitude in radius is used to resolve the flow over a wide range of spatial scales. We find that convection in the inner regions produces significant outward mass motions that carry away both the energy liberated by, and a large fraction of the mass participating in, the accretion flow. Although the instantaneous structure of the flow is complex and dominated by convective eddies, long time averages of the dynamical variables show remarkable correspondence to certain steady-state solutions. The two-dimensional structure of the time-averaged flow is marginally stable to the Høiland criterion, indicating that convection is efficient. Near the equatorial plane, the radial profiles of the time-averaged variables are power-laws with an index that depends on the radial scaling of the shear stress. A stress in which $\nu \propto r^{1/2}$ recovers the widely studied self-similar solution corresponding to an “ α -disc”. We find that regardless of the adiabatic index of the gas, or the form or magnitude of the shear stress, the mass inflow rate is a strongly increasing function of radius, and is everywhere nearly exactly balanced by mass outflow. The net mass accretion rate through the disc is only a fraction of the rate at which mass is supplied to the inflow at large radii, and is given by the local, viscous accretion rate associated with the flow properties near the central object.

Subject headings: a

accretion: accretion discs – black hole physics – hydrodynamics

1. Introduction

There is considerable interest in accretion flows which cannot lose internal energy through radiative cooling, since they may be relevant to accretion of diffuse plasma onto compact objects such as black holes and neutron stars. Steady-state solutions for the vertically-averaged radial structure of such flows have been developed within the context of self-similarity (for example, Ichimaru 1977; Begelman & Meier 1982; Narayan & Yi 1994; Abramowicz et al. 1995) assuming angular momentum transport is mediated by an anomalous shear “viscosity”. Solutions in which the mass accretion rate is constant with radius, and in which most of the gravitational binding energy liberated by accretion is stored as thermal energy (often called advection dominated accretion flows, or ADAFs) have been the focus of many recent studies motivated, for example, by the unusually low high-energy luminosity of some accreting black hole candidates (Narayan et al. 1998).

There is, however, a long standing question as to whether vertically-averaged solutions are indeed a good representation of the true multidimensional flow. For example, it is possible that the energy liberated by accretion could drive an outflow in the polar regions which accompanies accretion at the equator (Narayan & Yi 1994; 1995; Xu & Chen 1997). If the outflow carries a considerable fraction of the mass, energy, and angular momentum available in the accretion flow, it will have important consequences for the global nature of the solution (for example, the mass inflow rate at the equator can no longer be constant with radius). Recently, steady-state self-similar adiabatic inflow-outflow solutions (or “ADIOS”) have been developed in generality by Blandford & Begelman (1999a; 1999b, hereafter BB). Spectral models of such solutions have been calculated by Quataert & Narayan (1999). Despite the greater generality of the ADIOS models, there remains uncertainty as to how important properties of the outflow such as the mass loss rate and terminal velocity are determined.

Outflow from a non-radiative accretion flow will only be captured in a multi-dimensional treatment of the problem; angle-averaged solutions find only inflow in the inner regions (Ogilvie 1999). In a study of steady flows in thin discs, Urpin (1983; 1984) found that accretion at the surfaces of the disc could be accompanied by outflow along the equatorial (disc) plane. Gilham (1981) considered two-dimensional self-similar solutions which were separable in spherical polar coordinates. His solutions did not contain outflow, but they were also convectively unstable and therefore could not be steady.

An alternative technique for studying multidimensional non-radiative accretion flows is to use numerical methods to solve the time-dependent hydrodynamical equations directly. With such methods, a variety of problems related to accretion onto black holes have been studied. For example, the formation of rotationally supported thick tori from inviscid accretion of gas with various initial angular momentum distributions has been reported (Hawley, Smarr & Wilson 1984a; 1984b; Hawley 1986; see also Molteni et al. 1994; Ryu et al. 1995; Chen et al. 1997). More recently, an accretion flow driven by an anomalous “viscosity” around both non-rotating (Igumenshchev et al. 1996) and rotating (Igumenshchev & Beloborodov 1997) black holes has been simulated, revealing a variety of interesting features. The dynamic range of spatial scales in these latter simulations is too small for a direct comparison of the time-averaged state to the steady-state self-similar solutions discussed above, though more recently these authors have extended their calculations to include a much larger range in radius (Igumenshchev 1999; Igumenshchev & Abramowicz 1999, hereafter collectively referred to as IA99). These new calculations reveal

that bipolar outflows, strong convection, and quasi-periodic variability can result as the strength of the viscosity is varied.

Contemporaneous to the latest work of Igumenshchev, we have performed two-dimensional (axisymmetric) hydrodynamic calculations of non-radiative accretion flows which span over two orders of magnitude in radius. Our calculations begin with a well defined initial equilibrium state: a constant angular momentum “thick” torus. Because ultimately the accretion is driven by an assumed and *ad hoc* shear stress, we study several different forms and a wide range of amplitudes for this stress. We find that, for the models studied here, the instantaneous flow is dominated by strong small-scale convection in the inner regions. Some of the time-averaged properties of the flow are remarkably independent of the form of the shear stress, at least for the forms adopted here. In every case we find that at each radius, the mass flux carried inward by convective eddies is nearly exactly balanced by outward motions, so that the net mass *accretion* rate is small compared to the local mass *inflow* rate. For some forms of the anomalous stress, the regions of inflow and outflow are distributed equally throughout the disc, while for others the outflow occurs preferentially toward the poles, so that on the largest scales the time-averaged flow forms a global circulation pattern of inflow at the equator and slow outflow at the poles. None of our models show the production of powerful unbound winds. Most importantly, we find the net mass accretion rate through the disc is determined locally by the properties of the flow near the surface of the inner boundary; it is much smaller than the inflow rate at large radii.

Although our calculations have been pursued independently of the work of IA99, our formulation of the problem is very similar. In fact we differ only through the use of a different numerical method, a different representation of the shear stress (see §2.1), and different initial conditions (see §2.2). It is likely that the only difference of any importance is the representation of the shear stress. We compare our approach and results in more detail throughout this paper.

The paper is organized as follows. In §2 we describe our methods. In §3 we present the results of our hydrodynamical calculations. In §4 we discuss our results, while in §5 we summarize and conclude.

2. Method

2.1. The Equations of Motion

To compute the models discussed here, we solve the equations of hydrodynamics

$$\frac{d\rho}{dt} + \rho \nabla \cdot \mathbf{v} = 0, \quad (1)$$

$$\rho \frac{d\mathbf{v}}{dt} = -\nabla P - \rho \nabla \Phi + \nabla \cdot \mathbb{T}, \quad (2)$$

$$\rho \frac{d(e/\rho)}{dt} = -P \nabla \cdot \mathbf{v} + \mathbf{T}^2/\mu, \quad (3)$$

where ρ is the mass density, P the pressure, \mathbf{v} the velocity, e the internal energy density, and \mathbf{T} the anomalous stress tensor. The magnitude of the shear stress is determined by the coefficient μ ; we discuss the forms for μ used here below. The $d/dt \equiv \partial/\partial t + \mathbf{v} \cdot \nabla$ denotes the Lagrangian time derivative. A strictly Newtonian gravitational potential Φ for a central point mass M is used here. Using a pseudo-Newtonian potential (Paczynski & Wiita 1980) to approximate general relativistic effects in the inner regions is in principle straightforward but not of importance to the present investigation. We adopt an adiabatic equation of state $P = (\gamma - 1)e$, and consider models with both $\gamma = 5/3$ and $4/3$ (the latter value may provide a better, albeit crude, representation of the dynamics of a radiation dominated fluid). These equations are solved in spherical polar coordinates (r, θ, ϕ) .

The final term on the RHS of equations 2 and 3 represent anomalous shear stress and heating respectively added to drive angular momentum transport and accretion. It must be emphasized that the shear stress we wish to approximate is not the result of a true kinematic viscosity. In reality, we expect Maxwell stresses associated with MHD turbulence driven by the magnetorotational instability (MRI) to provide angular momentum transport in accretion flows (Balbus & Hawley 1998). Modeling such processes from first principles requires fully three-dimensional MHD calculations: an important and necessary step for future investigations but beyond the scope of this paper. To approximate the effects of magnetic stresses, we assume the azimuthal components of the shear tensor \mathbf{T} are non-zero and, in spherical polar coordinates, are given by

$$T_{r\phi} = \mu r \frac{\partial}{\partial r} \left(\frac{v_\phi}{r} \right), \quad (4)$$

$$T_{\theta\phi} = \frac{\mu \sin \theta}{r} \frac{\partial}{\partial \theta} \left(\frac{v_\phi}{\sin \theta} \right). \quad (5)$$

This form is similar to the shear stress in a viscous fluid, in which case $\mu = \nu \rho$ is the coefficient of shear viscosity, and ν the kinematic viscosity coefficient. We emphasize, however, that unlike a viscous fluid, we have assumed the non-azimuthal components of the shear stress are zero, because the MRI is driven only by the shear associated with the orbital dynamics, and therefore we do not expect it to affect poloidal shear to the same degree. Local three-dimensional MHD simulations of the properties of the MRI in the non-linear regime confirm that the azimuthal components of the Maxwell stress are indeed more than an order of magnitude larger than the poloidal components (e.g. Hawley, Gammie, & Balbus 1995; 1996; Brandenburg et al. 1995; Stone et al. 1996). IA99 use a shear stress which has a similar form to equations 4 and 5, except they also include the poloidal stress terms.

Although the local properties of the MRI in the nonlinear regime have been well studied, the radial scaling of the Maxwell stresses in a global MHD accretion flow is uncertain. Thus, we adopt several empirical forms for ν to study if and how the flow is changed. In particular, we consider models with (1) $\nu \propto \rho$, (2) $\nu = \text{constant}$, and (3) $\nu \propto r^{1/2}$. The first form is adopted primarily as a numerical convenience; it ensures the stresses are confined mostly to the torus where the density is large. In fact, as shown below, it results in a flow with constant density in the equatorial plane, which implies the shear stress per unit volume is nearly constant, i.e. it implies the solutions for the first and second forms of the stress should be similar. The third form for the shear stress corresponds

to the expectations of an “ α -disc” model. In the last two cases, the stress per volume is independent of all dynamical variables, thus the flow cannot adjust itself to change \mathbf{T} . Thus, we might expect models 2 and 3 to give quite different accretion solutions.

It is important to question whether approximating angular momentum transport in this manner rather than undertaking the requisite MHD calculations is worthwhile. Because “viscous” non-radiative accretion flows have been so widely discussed in the literature, it is useful to calculate their time-dependent hydrodynamical evolution over a large spatial scale both for comparison to studies of steady-state flows, and to serve as a baseline for future time-dependent MHD calculations. Because we find that the time-averaged properties of the flow are remarkably independent of the form of the shear stress, it is possible that some of the results found here will not be qualitatively different in an MHD calculation, provided the angular momentum transport is dominated by internal Maxwell stress (rather than external torques provided by global fields). Clearly MHD calculations are warranted to investigate these issues.

2.2. Initial Conditions

Our simulations begin with an equilibrium state consisting of a constant angular momentum torus embedded in a non-rotating, low-density ambient medium in hydrostatic equilibrium. The pressure and density in the torus initially are related through a polytropic equation of state $P = A\rho^\gamma$, so that the equilibrium structure of the torus is given by (Papaloizou & Pringle 1984)

$$\frac{P}{\rho} = \frac{GM}{(n+1)R_0} \left[\frac{R_0}{r} - \frac{1}{2} \left(\frac{R_0}{r \sin \theta} \right)^2 - \frac{1}{2d} \right]. \quad (6)$$

Here $n = (\gamma - 1)^{-1}$ is the polytropic index, R_0 is the radius of the center (density maximum) of the torus, and d is a distortion parameter which measures the shape of the cross-sectional area of the torus. Physical solutions to equation 6 require $d > 1$, with values near one giving small, nearly circular cross sections. Without loss of generality, we choose units such that $G = M = R_0 = 1$, so that the maximum density is

$$\rho_{max} = \left(\frac{1}{(n+1)A} \left[\frac{d-1}{2d} \right] \right)^n. \quad (7)$$

For given values of ρ_{max} , d and n , equation 7 determines A . In most cases we adopt $\rho_{max} = 1$, although in some models we specify the mass contained in the torus instead.

The ambient medium in which the torus is embedded has density ρ_0 and pressure $P_0 = \rho_0/r$. The mass and pressure of the ambient medium should be negligibly small; here we choose $\rho_0 = 10^{-4}$ so that the ratio of the mass in the ambient medium in $r < R_0$ to that in the torus M_t is $\sim 4 \times 10^{-4}$. Similarly, the ratio of the maximum pressure in the torus to the ambient pressure at $r = R_0$ is $\sim 5 \times 10^{-3}$. In order to guarantee an exact numerical equilibrium initially, we first initialize the density everywhere, and then integrate the radial equation of motion inwards from the outer boundary to compute the pressure using the numerical difference formula in our hydrodynamics code.

2.3. Numerical Methods

All of the calculations presented here use the ZEUS-2D code described by Stone & Norman (1992). No modifications to the code were required, apart from the addition of the shear stress terms. These terms are updated in an operator split fashion separately from the rest of the dynamical equations. For stability, these terms must be integrated using a time step which satisfies $\Delta t < \min(\Delta r, r \Delta \theta)^2 / \nu$, where Δr and $\Delta \theta$ are the radial and angular grid spacing, and the minimum is taken over the entire mesh. Whenever this requirement is smaller than the time step used for the hydrodynamic equations, we sub-cycle: that is we integrate the viscous terms repeatedly at the smaller timestep until one hydrodynamical timestep has elapsed.

Our computational grid extends from an inner boundary at $r = R_B$ to $4R_0$. In most simulations, we choose $R_B = 0.01R_0$, giving a spatial dynamic range over which an accretion flow can be established of two orders of magnitude. In some models we set $R_B = 0.005R_0$ with the outer boundary at $800R_B$, so that the grid extends nearly three orders of magnitude in radius. Such large dynamic ranges are essential for investigating an accretion flow in the self-similar regime, but are challenging because of the wide range in dynamical (orbital) timescales. For example, for the standard numerical resolution given below, one orbit of evolution at $r = R_0$ requires 10-15 hours on currently available workstations, while calculations at twice the standard resolution take more than 10 times longer.

In order to adequately resolve the flow over such a large spatial scale, it is necessary to adopt a non-uniform grid. We choose a logarithmic grid in which $(\Delta r)_{i+1}/(\Delta r)_i = N_r^{-1}\sqrt{10}$. This gives a grid in which $\Delta r \propto r$, with N_r grid points per decade in radius. Similarly, in order to better resolve the flow at the equator, we adopt non-uniform angular zones with $(\Delta \theta)_j/(\Delta \theta)_{j+1} = N_\theta^{-1}\sqrt{4}$ for $0 \leq \theta \leq \pi/2$ (that is the zone spacing is decreasing in this region), and $(\Delta \theta)_{j+1}/(\Delta \theta)_j = N_\theta^{-1}\sqrt{4}$ for $\pi/2 \leq \theta \leq \pi$. This gives a refinement by a factor of four in the angular grid zones between the poles and equator. Equatorial symmetry is not assumed. Our standard resolution is $N_r = 64$ and $N_\theta = 44$, giving a grid with a total size of 168×88 zones. We have also computed a high resolution model with $N_r = 128$ and $N_\theta = 80$, giving a grid with a total size of 334×160 zones.

We adopt outflow boundary conditions (projection of all dynamical variables) at both the inner and outer radial boundaries. We further set $T_{r\phi} = 0$ at the inner radial boundary. In the angular direction, the boundary conditions are set by symmetry at the poles (including setting $T_{\theta\phi} = 0$).

In some numerical simulations, numerical transport of angular momentum can limit the accuracy of the results. In fact, the consistent transport algorithms implemented in the ZEUS-2D code (Stone & Norman 1992) are specifically designed to reduce this effect. As a test, we have evolved a torus with $\nu = 0$ for 2 orbits at $r = R_0$. Apart from a slight smoothing of the sharp edges of the torus over 2-3 grid zones, we find no evolution. The angular momentum of the torus is conserved to one part in 10^6 , and the total rotational kinetic energy to one part in 10^3 .

We have also tested our implementation of the shear stress terms by comparing the evolution of the angle-integrated surface density at early times with the exact analytic solution for a thin viscous torus (e.g. Figure 1 of Pringle 1981). We find excellent correspondence between our numerical and the analytic solution up to a time of roughly 0.8

orbits, beyond which effects associated with the multidimensional nature of the flow in our simulations begin to become important.

3. Results

3.1. A Fiducial Model

Table 1 summarizes the properties of the simulations discussed here. Columns two through six give the coefficient of the shear stress ν , numerical resolution, radial extent of the numerical grid expressed as the ratio R_0/R_B , distortion parameter d of the torus, and adiabatic index γ respectively. The final two columns are the final time t_f at which each simulation is stopped (all times in this paper are reported in units of the orbital time at $r = R_0$), and the time-averaged mass accretion rate through the inner boundary measured near the end of the simulation, in units of the initial mass of the torus M_t per orbit.

We find models in which $\nu \propto \rho$ are the quickest to settle into a steady state; we discuss these models in detail to start. Runs A and B are low- and high-resolution simulations of a fiducial model with $\nu = 10^{-2}\rho$. Figure 1 plots the time evolution of the density in Run B. In each panel, gray shading is used to denote regions of the torus in which $v_r > 0$. Initially, the evolution is as predicted (Pringle 1981): most of the mass loses angular momentum and falls inward forming a wedge-shaped structure, while a small fraction of the mass gains angular momentum and moves outward. In fact, as indicated by the shading, the surface layers of the inner regions actually move outward – they form a Kelvin-Helmholtz (K-H) roll at the surface of the torus by $t = 0.5$. By $t = 1$ material has begun to accrete through the inner boundary, while outflow along the surface of the torus has carried the first K-H roll out to $r = 1.75$, and a second roll-up is forming at $r = 1$. Thereafter, the central wedge-shaped flow thickens considerably, so that by the end of the calculation the density contours in the inner regions are nearly radial. The wiggles in the contours in this region are caused by large amplitude density fluctuations in the flow associated with strong convective motions occurring at small radii. This convection drives a low-velocity outflow from the inner regions, in fact, all the material located at angles $\theta \gtrsim 45$ degrees from the equator is outflowing. This flow remains bound, however, so that it eventually cascades back onto the surface of the torus and merges with it in the outer regions. The radial pattern of shading at $t = 2.274$ in the inner regions, indicative of alternating columns of material with opposite sign in v_r , is another sign of large-scale convective flows.

Figure 2 is a plot of the time-history of the angle-integrated mass accretion rate \dot{M}_{acc} at $r = 0.01$ (i.e. the inner boundary), 0.05, and 0.1 in Run A, and at $r = 0.01$ in Run B, where

$$\dot{M}_{\text{acc}}(r) = 2\pi r^2 \int_0^\pi \rho v_r \sin \theta d\theta. \quad (8)$$

Because of the computational expense, Run B has not been evolved beyond 2.274 orbits. Note that the mass accretion rate through the inner boundary converges on the same value at both resolutions. Moreover, the time-averaged accretion rate is independent of radius at

Table 1: Properties of Simulations

| Run | ν | Resolution ^(a) | R_0/R_B | d | γ | t_f (orbits ^(b)) | $\dot{M}_{\text{acc}}(R_B)^{(c)}$ ($M_t/\text{orbit}^{(b)}$) |
|-------------------|------------------------|---------------------------|-----------|-------|----------|--------------------------------|--|
| A | $10^{-2}\rho$ | 64 | 100 | 1.125 | 5/3 | 4.325 | 1.0×10^{-3} |
| B | $10^{-2}\rho$ | 128 | 100 | 1.125 | 5/3 | 2.274 | 8.2×10^{-4} |
| C | $10^{-2}\rho$ | 64 | 200 | 1.125 | 5/3 | 1.947 | 5.0×10^{-4} |
| D | $10^{-2}\rho$ | 64 | 50 | 1.125 | 5/3 | 4.000 | 1.8×10^{-3} |
| E | $10^{-2}\rho$ | 64 | 100 | 1.125 | 4/3 | 2.155 | 1.6×10^{-3} |
| F | $5 \times 10^{-3}\rho$ | 64 | 100 | 1.042 | 5/3 | 3.539 | 9.1×10^{-4} |
| G | $5 \times 10^{-3}\rho$ | 64 | 100 | 1.042 | 4/3 | 1.391 | 1.9×10^{-3} |
| H | $10^{-3}\rho$ | 64 | 100 | 1.125 | 5/3 | 20.389 | 6.6×10^{-5} |
| I | $10^{-1}\rho$ | 64 | 100 | 1.125 | 5/3 | 0.593 | 3.0×10^{-3} |
| I' ^(d) | $10^{-1}\rho$ | 64 | 100 | 1.125 | 5/3 | 3.110 | 2.4×10^{-3} |
| J | 10^{-3} | 64 | 100 | 1.125 | 5/3 | 5.479 | 8.3×10^{-4} |
| K | $10^{-3}r^{1/2}$ | 64 | 100 | 1.125 | 5/3 | 13.6181 | 1.1×10^{-3} |

(a) grid points per decade in radius, (b) at $r = R_0$, (c) averaged over last orbit, (d) restarted from Run A

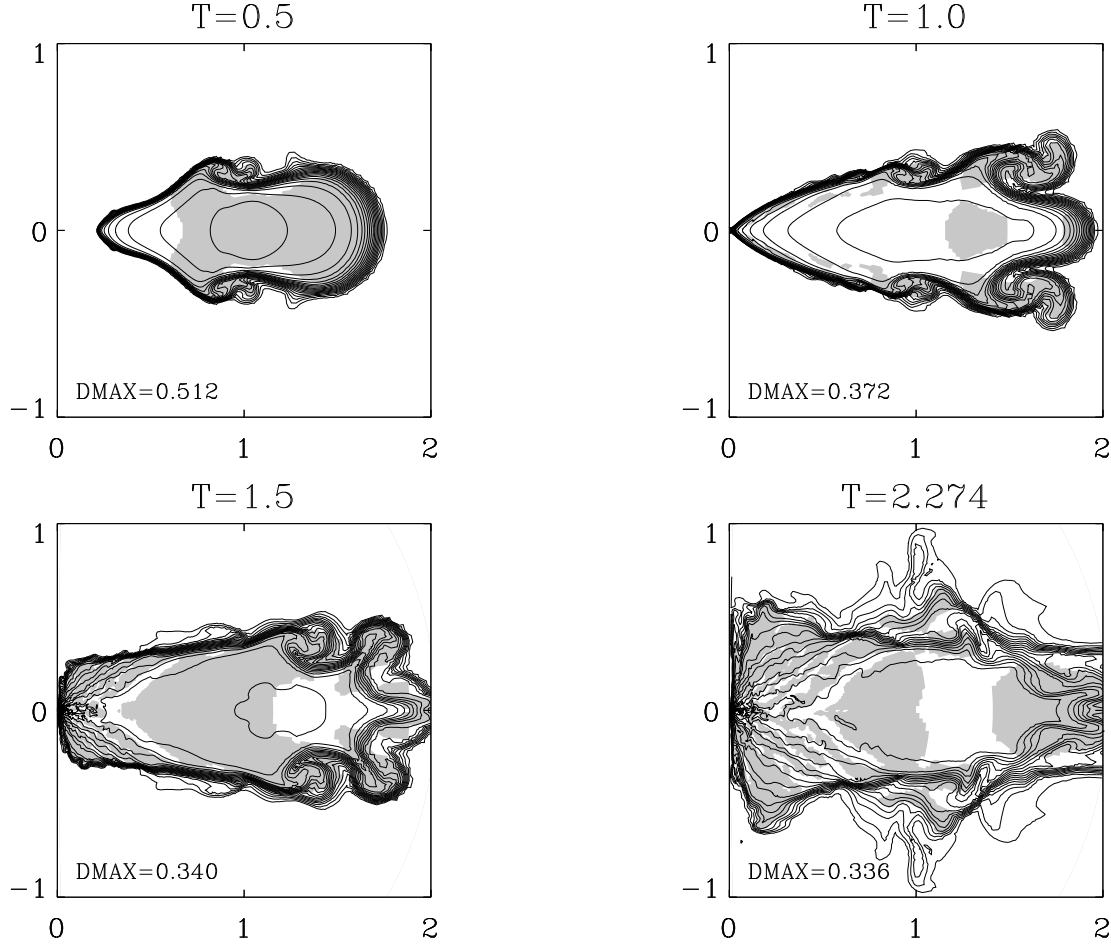


Fig. 1.— Evolution of the density in a fiducial model (Run B). Time is measured in units of the orbital time at $r = 1$. Twenty logarithmic contours are used between the density maximum (given in each panel) and 10^{-4} . The shaded regions have $v_r > 0$.

late times, indicating the flow has reached a steady state over at least one decade in radius. Because the plot shows the *integrated* accretion rate, it does not reveal the magnitude of the inflow near the equator or the outflow near the poles, but only the difference. This net mass accretion rate is very small, it would take $M_t/\dot{M} \approx 10^3$ orbits to accrete the entire torus. (Of course some material would never be accreted as required by energy and angular momentum conservation.)

To reveal the complex structure of the flow at small radii, in Figure 3 we plot snapshots of the density, entropy (for a non-radiating fluid) $S = \ln(P/\rho^\gamma)$, and angular momentum excess compared to Keplerian motion $\delta l = \rho(v_\phi r \sin \theta - \sqrt{r \sin \theta})$ at $t = 1.95$ for the central region $r < 0.1$. The complexity of the flow on these scales is evident. Overall, the density is strongly stratified from the poles to the equator, however on small scales large amplitude fluctuations associated with convection dominate the image. Several regions of dense blobs and filaments (which move inward), and low density bubbles (which move outward) are clearly evident. Note that at some radii, the angular position of the density maximum is displaced far from the equator, an indication of how strongly the convective motions dominate the flow. The entropy plot shows the generic result for a non-radiative accretion flow that S is maximum along the poles (where the density is a minimum), and smallest along the equator. However, once again the dominant pattern in the image are the bubbles and filaments associated with convection. Finally, the plot of δl shows that overall, the flow near the poles has an excess of angular momentum compared to Keplerian, while near the equator large amplitude fluctuations of both excess and deficit are present. A plot of the instantaneous radial velocity on these scales is complex, revealing that both inflow and outflow occurs at some place along most radial slices. However, there is an overall pattern to the flow: inflow dominates near the equator and outflow near the poles. Comparison of the three images demonstrates that, as one would expect, regions of highest density (which are observed to move inward) have low S and a deficit of angular momentum, while bubbles of low density (which are observed to move outwards) have high S and an excess of angular momentum. A detailed comparison of the properties of convection in a rapidly rotating flow such as being studied here with the known properties of stellar convection (e.g. Mestel 1999) would be fruitful, but will not be discussed further here.

In order to investigate the time-averaged properties of the flow, in Figure 4 we plot contours of a number of time-averaged quantities, including the specific angular momentum $L = v_\phi r \sin \theta$, and the Bernoulli function $B \equiv v^2/2 + \gamma P/(\gamma - 1)\rho - r^{-1}$. The latter is shaded in regions where $B < 0$. These averages are constructed from 139 equally spaced data files between orbits 2.0 and 2.278. The time-averaged variables form remarkably simple patterns compared to the instantaneous snapshots (c.f. Fig. 3). In each case the contours form smooth curved surfaces which are symmetric with respect to the equator. The ordering of the variables according to the shape of their contours (from concave to convex with respect to an outward radial norm) is ρ , P , r , Ω , R , L , B , and S , where r and R are spherical and cylindrical radial coordinates respectively. Contours of the last three variables are in fact virtually parallel, except for contours of $B < 0$. (Note in the region shown the contours of ρ are nearly radial, however since they must close at large r we consider this as an extreme limit of concavity.) This ordering is precisely that expected for stability against the Høiland criterion (Begelman & Meier 1982; BB), thus we conclude the mean state is marginally stable. The convective motions are therefore so efficient as to drive the mean flow to marginal stability (since the instantaneous structure is clearly *unstable*). We note the shading of B indicates that in a time-average sense, $B < 0$ for material near the equator (where there is inflow), while $B > 0$ nearer the poles (where there is outflow).

The instantaneous structure of B may contain large bubbles of positive value embedded in negative values near the midplane.

Figure 5 plots the radial structure of the time-averaged flow near the equatorial plane in Run B, averaged from $\theta = 84$ to 96 degrees. The time-averaging used to construct the plot is identical to that used in Fig. 4. It is clear that each variable in the plot can be described by a radial power law, with $\rho \propto r^0$, $P \propto r^{-1}$, $v_\phi \propto r^{-1/2}$, and $v_r \propto r^{-1}$. Note the rotational velocity never falls below 0.9 times the Keplerian value, except directly next to the inner boundary. The power-law index of P is somewhat uncertain: $P \propto r^{-1}$ is really only a good fit for $r < 0.1$. If we adopt the ansatz that the Bernoulli function is zero at all radii near the equatorial plane (justified by the results shown in Fig. 4), and that the kinetic energy is dominated by the rotational velocity (which is nearly Keplerian), one would predict

$$\gamma P / \rho = \frac{1}{3r} \quad (9)$$

for $\gamma = 5/3$. In fact, equation 9 provides an approximate fit to the radial profile of the time-averaged $C_s^2 \equiv \gamma P / \rho$.

The result that $v_r \propto r^{-1}$ indicates the solution is not strictly self-similar. Since at $r = 1$ the ratio $v_r / v_\phi \sim 10^{-2.5}$, the solution implies (if continued inward) that $v_r \sim v_\phi$ at $r \sim 10^{-5}$. We expect at this point the flow will change qualitatively. The particular scaling of the radial velocity with radius in this flow undoubtedly is related to the form of the shear stress used in this model, $\nu \propto \rho \propto r^0$. We note that since (from Fig. 5) the ratio $C_s^2 / \Omega \approx 0.3r^{1/2}$, it is not possible to characterize the shear stress by a constant $\alpha_{eff} = \nu \Omega / C_s^2$. Instead, $\alpha_{eff} \approx 10^{-2} r^{-1/2}$.

Figure 6 plots the radial structure of the time-averaged and angle-integrated mass inflow and outflow rates (\dot{M}_{in} and \dot{M}_{out} respectively), defined as

$$\dot{M}_{in}(r) = 2\pi r^2 \int_0^\pi \rho \min(v_r, 0) \sin \theta d\theta \quad (10)$$

$$\dot{M}_{out}(r) = 2\pi r^2 \int_0^\pi \rho \max(v_r, 0) \sin \theta d\theta \quad (11)$$

as well as the net mass accretion rate \dot{M}_{acc} defined in equation 8. Clearly $\dot{M}_{acc} = \dot{M}_{out} + \dot{M}_{in}$. To construct the plot, we time average the integral (rather than integrating the time-averages) using the same data as in Fig. 4. It is evident that both \dot{M}_{in} and \dot{M}_{out} increase roughly in proportion to r . However, the difference between the two (\dot{M}_{acc}) is constant with radius and is roughly equal to the local mass accretion rate expected for a thin, viscous disc calculated using the properties of the flow near the inner boundary, that is $\dot{M}_{acc} \approx \pi \nu (R_B) \Sigma(R_B)$. Using the known form of the stress $\nu = 10^{-2} \rho$, and the result from our simulations (see Figs. 5 and 7) that $\rho \approx 0.2 \sin \theta$ to compute $\Sigma(R_B)$ gives a viscous mass accretion rate which is within a factor of two of the measured \dot{M}_{acc} .

Figure 7 plots the angular structure of the time-averaged flow at radial positions of $r = 0.02, 0.05, 0.1$, and 0.2 , again using the same time-averaging as in Fig. 4. The angular structure of both the density and pressure shows smooth variation from the poles to equator, with the amplitude of ρ virtually identical at each radius and the amplitude of P dropping as r^{-1} . The radial velocity is negative over most θ at $r = 2R_B$. At larger r

there are still large variations in v_r , despite the large amount of data used to construct the time-average. The average v_r is slightly negative within about 30 degrees of the equator, and strongly positive within 50 degrees of the poles. The rotational velocity v_ϕ is nearly constant with θ at every radial position, so that L varies as $\sin \theta$. From the plots it is difficult to distinguish a surface that might be used to define the accretion disc as opposed to the polar outflow. Crudely, a surface might be defined near $\theta = 45$ degrees where the time-averaged radial velocity changes sign. Alternatively, the surface of $B = 0$ in the fifth panel of Fig. 4 might be considered to define a disc.

A plot of the time-averaged angular velocity reveals v_θ is negative (positive) within 50 degrees of $\theta = 0$ ($\theta = \pi$), and nearly zero elsewhere. The angular and radial pattern of v_r and v_θ indicate that for Run B, there is a weak global circulation pattern consisting of slow radial infall near the equator, and faster polar outflow above $\theta \approx 45$ degrees. The average velocity of the circulation is much smaller than the instantaneous fluctuations, especially near the equator.

The increase of \dot{M}_{in} and \dot{M}_{out} with radius indicates most of the mass which flows inward near the equatorial plane eventually flows outward towards the poles. Fundamentally, this result seems to be a consequence of strong convection in the inner regions which, when combined with diffusion on the smallest scales, serves to mix the specific entropy of the fluid. Thus, outflowing material has only a slightly larger specific entropy than the rest of the material, so that it is very inefficient at carrying away energy liberated by the infalling gas (BB). The result is that a large amount of outflowing mass is required to remove the energy liberated by the small accretion rate.

To confirm that our solution is independent of the location of the inner boundary, we have calculated the evolution of two additional models, one with $R_B = 0.005$ (Run C), and the other with $R_B = 0.02$ (Run D), but otherwise identical to Run A. The final, time-averaged \dot{M}_{acc} through the inner boundary measured from these runs is listed in Table 1. The results are consistent with $\dot{M}_{\text{acc}} \propto r$. Since for the particular accretion flow established in our simulations the viscous accretion rate is proportional to r , this result again indicates that the net mass accretion rate is determined locally at the surface of the central object. The details of the flow in Runs C and D are similar to Run A, we find the same radial and angular structure of the time-averaged flow as is shown in Figs. 4-7. In particular, the outflowing material is still bound, and has the same total energy as in Run A, and therefore stagnates at roughly the same radial position as the flow shown in the last panel of Fig. 1. Making the inner boundary smaller does not lead to the production of a more energetic outflow. Of course, varying the location of the inner boundary is equivalent to moving the initial location of the torus either closer to or farther from the central point mass. Since most of the gravitational energy is liberated near the central object, we should not expect substantial changes in the flow if the torus starts at $200R_B$ as opposed to $100R_B$, as is indeed observed.

We have studied the direction of the time-averaged advective flux of mass, energy, and angular momentum, and the flux of L transported by shear stresses in Run B. We find the first three are nearly identical, thus in Figure 8 we show a vector plot of only $\dot{M} = 2\pi r^2 \rho v_r \sin \theta$ for the same 139 data files as used to construct Figs. 4-7. To further reduce the noise in the data, we have averaged together the fluxes on either side of the equator. Even so, the direction of the inflow does not form smooth streamlines. Overall, there is a quasi-radial inflow within $\theta \sim 45$ degrees, and a more nearly radial outflow above that (although, consistent with the profile of the time-averaged angular velocities mentioned

above, the mass flux vectors are more polar than equatorial). Note from Fig. 8 that one could also use the change in sign of the radial component of the average mass flux vectors to crudely define a surface to the disc at $\theta \sim 45$ degrees. Although not plotted, the viscous flux of angular momentum is radial within the inflowing regions, and away from the poles in the outflow.

The accretion flow which emerges from these calculations must be driven by angular momentum transport associated with the anomalous shear stress. This is clearly demonstrated by setting the shear stress to zero once the mass accretion rate has reached a steady-state. When Run A is continued for another orbit with $\nu = 0$, the mass accretion rate drops by an order of magnitude within 0.1 orbits, the convective motions die away, and the torus settles into a new two-dimensional hydrostatic equilibrium with a nearly Keplerian rotation profile near the equator.

It can also be demonstrated that the thermal heating due to the anomalous shear stress plays a fundamental role in producing convection and mass outflow. If we repeat the fiducial model with the heating term (last term in equation 3) removed, we find a high-velocity, ordered infall is produced with no small-scale convective motions.

We have studied the effect of varying the adiabatic index γ on the properties of the flow. Run E listed in Table 1 has $\gamma = 4/3$, but otherwise is identical to the fiducial model Run A (a different value of A must be chosen in order to keep M_t fixed – this increases the maximum initial density in the torus). We find that apart from being slightly more compact in the equatorial plane (the opening angle of the accretion being closer to 30 degrees) the detailed properties of the solution (for instance the radial scaling of time-averaged variables) do not change significantly compared to Run A. The rotational velocity is still very nearly Keplerian, and $\rho \propto r^0$ and $v_r \propto r^{-1}$. Most significantly, we still find $\dot{M}_{\text{in}} \propto r$ in this simulation. The mass accretion rate through the inner boundary listed in Table 1 is increased in Run E compared to A; it is a small fraction of $\dot{M}_{\text{in}}(R_0)$ and is consistent with the local, viscous accretion rate at the inner boundary.

Finally, to study the effect of the shape of the initial torus, we have computed two models with $d = 1.042$, one with $\gamma = 5/3$ (Run F) and one with $\gamma = 4/3$ (Run G). Once again, M_t is kept fixed between these models by choosing an appropriate value for A . The smaller value of d used in these models gives the torus in the initial state a cross-sectional diameter about one half the value in Run A. We find no qualitative change in the solution compared to Run A. In particular, the outflow is driven to the same radial position (but no farther), indicating that the initial thermal energy is not important in the outflow. In both cases, the flow is dominated by convection in the inner regions, with time-averaged radial profiles for each variable that obey the same radial scalings as found for Run A. The $\gamma = 5/3$ (Run F) model has a steady-state mass accretion rate identical to Run A, while in the $\gamma = 4/3$ (Run G) model the accretion rate is increased by the same amount as Run E.

3.2. Effect of varying the amplitude of the Shear Stress

We have calculated the evolution of two models in which $\nu = 10^{-3}\rho$ and $\nu = 10^{-1}\rho$ (i.e., the shear stress is either ten times smaller or larger than in the fiducial model respectively).

These models are labeled as Runs H and I in Table 1. Each model is computed at the standard resolution of 64 grid points per decade in radius. Together with Run A, they form a set of models which span two orders of magnitude in amplitude of the anomalous shear stress.

At low values of the shear stress (Run H), the evolution to a steady accretion flow proceeds much more slowly than in the fiducial model, as one would expect. Thus, it takes roughly 20 orbits of the torus for \dot{M}_{acc} to converge to a steady value. This value (final column in Table 1) is roughly fifteen times smaller than Run A, although for a viscous disc one expects the mass accretion rate to be directly proportional to ν . The discrepancy can be attributed to the fact that the density at the equator is about 2/3 the value in Run A. The two-dimensional structure of the time-averaged flow in Run H is very similar to that shown in Figure 4 for Run A. The radial scaling of all variables near the equator also follow the results of Run A closely, i.e. $\rho \propto r^0$, $P \propto r^{-1}$, $v_\phi \propto r^{-1/2}$, and $v_r \propto r^{-1}$. The ratio of $v_r/v_\phi \sim 10^{-3}$ at R_0 , slightly smaller than Run A. Once again, the inner regions of the flow are dominated by convective motions which drive a significant outward mass flux that carries away most of the energy liberated by accretion. The mass inflow rate once again scales as $\dot{M}_{\text{in}} \propto r$.

At high values of the shear stress (Run I), the evolution of the torus becomes very dynamic. In fact, the initial infall of material from the torus becomes nearly supersonic, reaching the rotation axis after only 0.15 orbits. This rapid infall creates a high pressure as material reflects off the rotation axis, resulting in the ejection of some matter along the poles. Convective motions begin within $r < 0.1$ after 0.2 orbits, at which point the flow attempts to settle into the same equatorial-inflow polar-outflow solution observed in Run A. However, the mass accretion rate is marked by large amplitude fluctuations throughout the evolution of Run I, leading to a time-averaged value only 3 times larger than Run A. The time-averaged radial scaling of all variables shows the same dependences on r for all variables as observed in Run A for $r > 0.1$, however for $r < 0.1$ some variables diverge from simple power-law behavior. For example, both the rotational and radial velocity becomes flat for $r < 0.04$. At the inner edge, the ratio of $v_r/v_\phi \approx 0.5$, and $v_\phi/C_s \approx 0.5$ (note for Run A this latter ratio ~ 1.2). These ratios indicate the flow has deviated from strictly Keplerian rotation, and that radial pressure gradients are playing an important role in the radial structure of the flow. Despite the fact that the flow at such large values of the shear stress (the “effective- α ” of Run I at the inner boundary is $\alpha_{\text{eff}} = \nu\Omega/C_s^2 \approx 0.1$) is qualitatively different in the inner regions compared to the fiducial model, we still observe very low mass accretion rates through the inner boundary compared to the mass inflow rate at large radii $\dot{M}_{\text{in}}(R_0)$.

Because the violent initial collapse of the torus may be interfering with the establishment of a steady accretion flow, we have also calculated a model which begins from the final state of Run A, but with a shear stress which is slowly increased until $\nu = 10^{-1}\rho$. That is, starting from time 4.325 in Run A, the model is evolved for roughly one orbit with $\nu = 2 \times 10^{-2}\rho$, one orbit with $\nu = 5 \times 10^{-2}\rho$, and finally one orbit with $\nu = 10^{-1}\rho$. The final time-averaged mass accretion rate in the model (Run I') given in Table 1 is only a factor of 2.4 larger than the initial accretion rate measured in Run A. In fact, almost no change in the accretion rate is observed after the final increase in ν , indicating that the mass accretion rate is limited at large values of the stress. The radial profiles of each variable in Run I' follow power laws over a wider range in radii, with v_r and v_ϕ becoming flat only over $r < 0.02$. The ratio of $v_r/v_\phi \approx 0.3$ at the inner edge, while $v_\phi/C_s \approx 0.7$. The flow in

Run I' is again marked by large amplitude fluctuations in the mass accretion rate. Thus, we conclude that at high values of the shear stress, the flow deviates from a rotationally supported disc due to radial pressure support. However, we emphasize that strong mass outflow and convection are still important.

Finally, we note that IA99 have also studied the effect of varying the amplitude of the shear stress on non-radiative accretion flows. At low values of ν , they find strong, small-scale convective eddies dominate the flow, in accordance with the results presented here. At large ν (much larger than the largest value we have studied here), they find the flow becomes more laminar, and produces a bipolar outflow structure. Qualitatively, our results are in agreement, although there is an indication of stronger convection in our solutions at large ν . It is possible that the poloidal shear stress used by IA99 may partially suppress convection in this case.

3.3. Effect of Varying the Form of the Shear Stress

The last two models listed in Table 1 have been computed with entirely different forms for the anomalous shear stress than Runs A through I discussed above. Run J uses a spatially constant stress, whereas Run K uses a stress proportional to $r^{1/2}$. In both models, the amplitude is normalized to give roughly the same stress at R_0 as in Run A (about 10^{-3} since $\rho \sim 0.2$ at late times). We use Runs J and K to investigate the effect of changing the form (rather than amplitude) of the stress on the resulting flow.

Since, once a steady-state is achieved in the inner regions, the accretion flow in which $\nu \propto \rho$ has constant density along the equatorial plane (leading to a constant shear stress with radius), we expect the flow in Run J to be similar to Run A. Indeed, we find that in Run J the mass accretion rate eventually saturates at approximately the same value as Run A. The flow is once again dominated by large amplitude convection motions in the inner regions. Most importantly, the time-averaged two dimensional and radial structure of the flow is similar to that found in Run A. In particular, we again find $\rho \propto r^0$, $v_r \propto r^{-1}$, and $\dot{M}_{\text{in}} \propto r$, while the ratio $v_r/v_\phi \sim 10^{-2.5}$ at $R = R_0$. Perhaps the only significance of this result is that although the shear stress in the outflowing material is greatly increased in Run J compared to Run A (because of the variation in density with θ) the details of the inflow-outflow solution have not been affected. Both the same amplitude for the mass accretion rate and the same radial scaling of the time-averaged solution are obtained.

In Run K the shear stress is given a fixed radial scaling which differs from the profile of the stress eventually established in Runs A and J; thus we might expect a quite different flow pattern to result. The mass accretion rate eventually saturates in Run K after 10 orbits at a value consistent with Run A. Figure 9 plots two-dimensional contours of time-averaged variables in Run K constructed from 33 equally spaced data files between orbits 12.0 and 13.6. The general shape of the contours (from concave to convex with respect to an outward norm at the equator) follows the same pattern as observed in Run B (Fig. 4). In particular, the systematic trend in the shapes indicates that once again, strong convection drives the time-averaged flow into a marginally stable state. However, there are important differences in the solution; in particular the density at the midplane is

now clearly decreasing with radius, while the Bernoulli function is negative over nearly the entire domain. The instantaneous structure of each variable at any time after the flow has reached a steady accretion rate is close to that shown in Figure 3 for Run B – namely large amplitude fluctuations around the mean values shown in Figure 9 associated with strong convection.

Figure 10 plots the radial structure of the flow in Run K averaged between angles of 85 and 95 degrees, using the same time averaged data as used to construct Figure 9. Once again, each variable is seen to be best fit by a power-law scaling with radius, with $\rho \propto r^{-1/2}$, $P \propto r^{-3/2}$, $v_\phi \propto r^{-1/2}$, and $v_r \propto r^{-1/2}$. Note the scaling of ρ , P , and v_r differ from that found for Run B; in this case the solution is indeed self-similar. The radial scaling of C_s^2 follows equation 8 reasonably well.

Figure 11 plots \dot{M}_{in} , \dot{M}_{out} , and \dot{M}_{acc} for Run K using the same time-averaging as in Figure 9. While both the mass inflow and outflow rates increase rapidly with r , they do so less steeply than in the fiducial model (c.f. Fig. 6): here $\dot{M}_{\text{in}} \propto r^{3/4}$ roughly. The net mass accretion rate \dot{M}_{acc} is remarkably constant throughout the flow, and has a value consistent with the viscous accretion rate for the properties of the flow near the inner boundary.

Figure 12 plots the angular structure of the time-averaged flow in Run K at radial positions of $r = 0.02, 0.05, 0.1$, and 0.2 , again using the same time-averaging as in Fig. 9. The angular structure of both the density and pressure shows smooth variation from the poles to equator, with the amplitude of both dropping with radius. Unlike the profiles of the radial velocity for the fiducial model Fig. 7, v_r averages to almost zero over most angles in Run K. Like the radial velocity, the time-averaged angular velocity is almost zero over most angles. As in Fig. 7, the rotational velocity v_ϕ is nearly constant with θ at every radial position, so that L varies as $\sin \theta$. Note that the profile at $r = 2R_B$ (solid line each panel) may be affected by numerical resolution near the poles: Run K is computed at only half the resolution of Run B. Comparison of the structure of the solution in Runs A and B (the same model computed at different resolutions) indicate that within $r = 2R_B$ material can fill in the gap near the poles in the lower resolution simulations. The radial and angular profiles of v_r and v_θ indicate there is no global circulation pattern in Run K, instead inflow and outflow are evenly distributed throughout the disc. In this respect, the flow is closer in analogy to a rapidly rotating star than an accretion disc, in that thermal energy is produced deep in the interior and is convected outwards at all angles.

4. Discussion

Our major finding is that, independent of the equation of state of the gas, and independent of the magnitude and functional form of the shear stress, the angle-integrated mass inflow rate strongly increases with radius, $\dot{M}_{\text{in}} \propto r$ for Runs A-J, and $\dot{M}_{\text{in}} \propto r^{3/4}$ for Run K. In every case, the mass inflow is balanced by a nearly equal mass outflow, so that the actual accretion rate onto the central object $\dot{M}_{\text{acc}}(R_B)$ is only a fraction of the canonical accretion rate $\dot{M}_{\text{in}}(R_0)$ which should be generated by the torus at radius R_0 for the given

shear stress,

$$\dot{M}_{\text{acc}}(R_B)/\dot{M}_{\text{in}}(R_0) \sim (R_B/R_0)^q \quad (12)$$

where $q = 1$ (Runs A-J) or $q = 3/4$ (Run K). For most of the models presented here, $R_B/R_0 = 0.01$, although we find this scaling also applies over a range of this ratio. The net mass accretion rate through the flow is constant with radius (as it must be for a steady state) and is consistent with the local viscous accretion rate given by the properties of the flow near the inner boundary.

Although this result is independent of the nature of the shear stress, the detailed properties of the solution do in fact change according to the functional form of the stress. For example, models in which the shear stress per unit volume ν is constant give $\rho \propto r^0$ and $v_r \propto r^{-1}$, whereas models in which $\nu \propto r^{1/2}$ give $\rho \propto r^{-1/2}$ and $v_r \propto r^{-1/2}$. In fact, these scalings can be understood directly from the equations of motion, using the known properties of the solutions. For example, using the fact that the time-averaged rotational velocity is nearly Keplerian ($v_\phi = r^{-1/2}$) and symmetric across the equatorial plane, the ϕ -component of the momentum equation in spherical polar coordinates can be written (assuming steady state) as

$$\left(\frac{3}{2}\right)^2 \frac{\nu}{r^2} + \left(\frac{3}{2}\right) \frac{\nu}{r} \frac{1}{\rho} \frac{\partial \rho}{\partial r} + \left(\frac{3}{2}\right) \frac{1}{r} \frac{\partial \nu}{\partial r} + \frac{v_r}{2r} = 0. \quad (13)$$

For this equation to hold over many orders of magnitude in radius, all terms must scale with r in the same way. Thus, one sees immediately that for $\nu = \text{constant}$, $v_r \propto r^{-1}$, whereas for $\nu \propto r^{1/2}$, $v_r \propto r^{-1/2}$.

As discussed in §3, the solutions computed here also fit the condition that the time-averaged Bernoulli function B is approximately zero in the equatorial plane. For nearly Keplerian rotation with negligible polar velocities, this implies $P/\rho = (\gamma - 1)/2\gamma r$ (equation 9). Using this condition in the energy equation, combined with the continuity equation and the angular momentum equation given above, it is possible to predict not only the radial scalings, but also the amplitudes of the flow variables. We find such predictions are only within a factor of a few of the measured time-averaged flow variables plotted in Figs. 5 and 10. It is possible this discrepancy arises because of the difference between constructing nonlinear functions of time-averaged variables versus the time-average of the functions themselves.

Because almost all of the inflowing material at any particular radius in the flow is balanced by a nearly equal and opposite outflow which carries away the energy liberated by accretion, the solutions found here may be considered as the “maximally inefficient” accretion solution, one limit of the ADIOS solutions discussed by BB. We emphasize, however, that we do not see powerful, unbound winds in our flows, rather only slow, outflow associated with convective eddies. Our flows are inefficient because vigorous convection in the flow quickly equalizes the specific entropy of all the gas, thus in order for a small fraction of the gas to lose energy and accrete inwards, a large fraction must carry off that energy in a slow outflow. There may be some physical effects (such as torques from strong magnetic fields) that can drive much faster outflows that have a much higher specific energy. In this case, it is possible that a smaller fraction of the inflowing material will be lost to the outflow, and therefore \dot{M}_{in} may not be as steep as r (BB). Equally important, magnetic fields will regulate angular momentum transport through the magnetorotational instability,

and thus in MHD the gas does not require an *ad hoc* anomalous shear stress to accrete. Fully MHD calculations that can capture both of these effects are underway.

Besides the neglect of magnetic fields, our solutions may also be limited by the assumption of axisymmetry. In a fully three-dimensional flow, angular momentum can be carried outwards by global waves (for example, our initial state is unstable to a non-axisymmetric global instability, Papaloizou & Pringle 1984), and perhaps through the action of radial convection. However, we do not expect these effects to change the qualitative nature of the axisymmetric solutions found here. Fully three-dimensional simulations are also underway to test this expectation.

Of course, having $\dot{M}_{\text{in}} \propto r$ has important implications for the observations of accreting compact objects (BB; Quataert & Narayan 1999) – the apparent lack of high-energy emission from such objects may be a result of the vanishingly small accretion rate in the inner regions. It is equally interesting to determine the long term evolution of matter accreting onto compact objects through the non-radiative accretion flow solutions presented here. The ultimate fate of the outflowing material depends on whether it is able to cool at large radii and thereby rejoin the accretion flow (except for the small fraction needed to carry away the angular momentum). It is feasible that such a recycling process may lead to an increase in the density in the inflowing material. Potentially, this can lead to an increase in the radiative efficiency, and could make the flow transition to a thin disc with a much larger accretion rate. Most of the mass accreted by the central object may be accumulated through such episodic bursts of accretion. We must express a strong word of caution at this point, however. We have presented solutions over two orders of magnitude in radius for at most twenty orbits of the outer regions. Such evolutionary effects will require understanding the solutions over five or more orders of magnitude in radius for thousands of orbits of the outer regions.

5. Conclusions

We have investigated the properties of non-radiative rotating accretion flows by carrying out a set of numerical two-dimensional (axially symmetric) hydrodynamical experiments using a simple starting configuration and a set of well-defined boundary conditions. We start with all the mass rotating in a torus in hydrodynamic equilibrium at radius $R_0 = 1$. We allow small (in the sense that the induced flow velocities are small compared to the rotational velocities) anomalous shear stresses to act on the flow. We set a purely accreting inner boundary at (for most of our models) a radius of $R_B = 0.01$. All energy deposited in the fluid by shear stresses is retained by the fluid, and not radiated. A spherical polar grid with logarithmically spaced zones is used to resolve the flow over more than two decades in radius.

We find that in the inner regions, the flow becomes strongly convective, and in fact convective motions dominate the instantaneous structure of the flow. This convection produces outward moving fluid elements (with high entropy, low density, and an excess of angular momentum compared to rotation at the local Keplerian value) at all angles, including near the equator. The outflowing material removes mass, angular momentum, and

most importantly energy from the accretion flow. However, the strong convection combined with diffusion on small scales mixes the specific entropy of the fluid very efficiently, which means that a very large mass loss rate is required to remove enough energy to allow some fluid to accrete.

Despite the strong time-dependence of the solution, long time-averages of the dynamical variables show remarkable correspondence to steady-state solutions. Two-dimensional contours indicate the time-averaged flow is marginally stable to the Høiland criterion. Radial profiles of the variables are all power-laws over nearly the entire domain. The rotation profiles are always nearly Keplerian (except for very large values of the shear stress when, in the inner regions, pressure gradients become substantial).

Perhaps the most important result of this study is that the mass accretion rate through the inner boundary is a small fraction of the angle-integrated mass inflow rate at large radii. The net mass accretion rate through the disc is consistent with the viscous accretion rate appropriate to the conditions in the flow at the surface of the central object. Most of the inflowing mass at large radii eventually becomes part of the outflow driven by convection. This result is independent of the adiabatic index of the gas, or the magnitude or form of the anomalous shear stress.

Qualitatively, our results are in agreement with those of Igumenshchev (1999), who has undertaken a similar study using different numerical methods, for low values of the shear stress. If confirmed by more realistic three-dimensional and MHD calculations, this result has important implications both for the spectrum and luminosity of accreting compact objects, and the long term evolution of accretion flows.

Acknowledgments: We thank Roger Blandford for many stimulating discussions and comments on earlier drafts of this paper, and an anonymous referee for helpful suggestions. JS gratefully acknowledges financial support from the Institute of Astronomy, and from NSF grant AST-9528299 and NASA grant NAG54278. MB acknowledges support from from NSF grants AST-9529175 and AST-9876887, and a Guggenheim Fellowship. This research was supported in part by the National Science Foundation under Grant No. PHY94-07194.

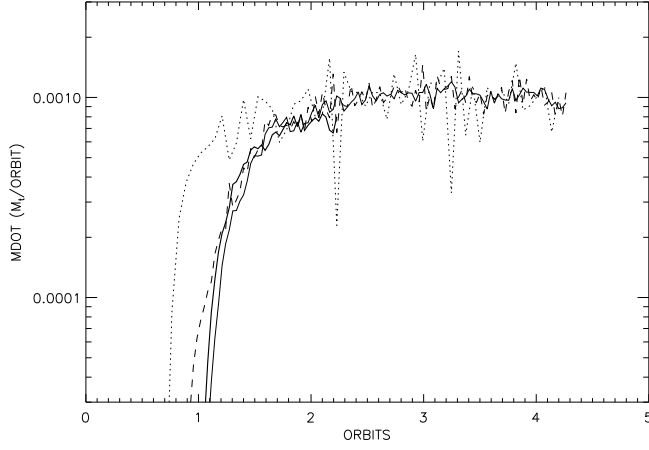


Fig. 2.— Total mass accretion rate at $r = R_B$ (solid line), $r = 5R_B$ (dashed line), and $r = 10R_B$ (dotted line) in the fiducial model (Run A). The bold solid line is the total mass accretion rate at $r = R_B$ in the high resolution simulation (Run B).

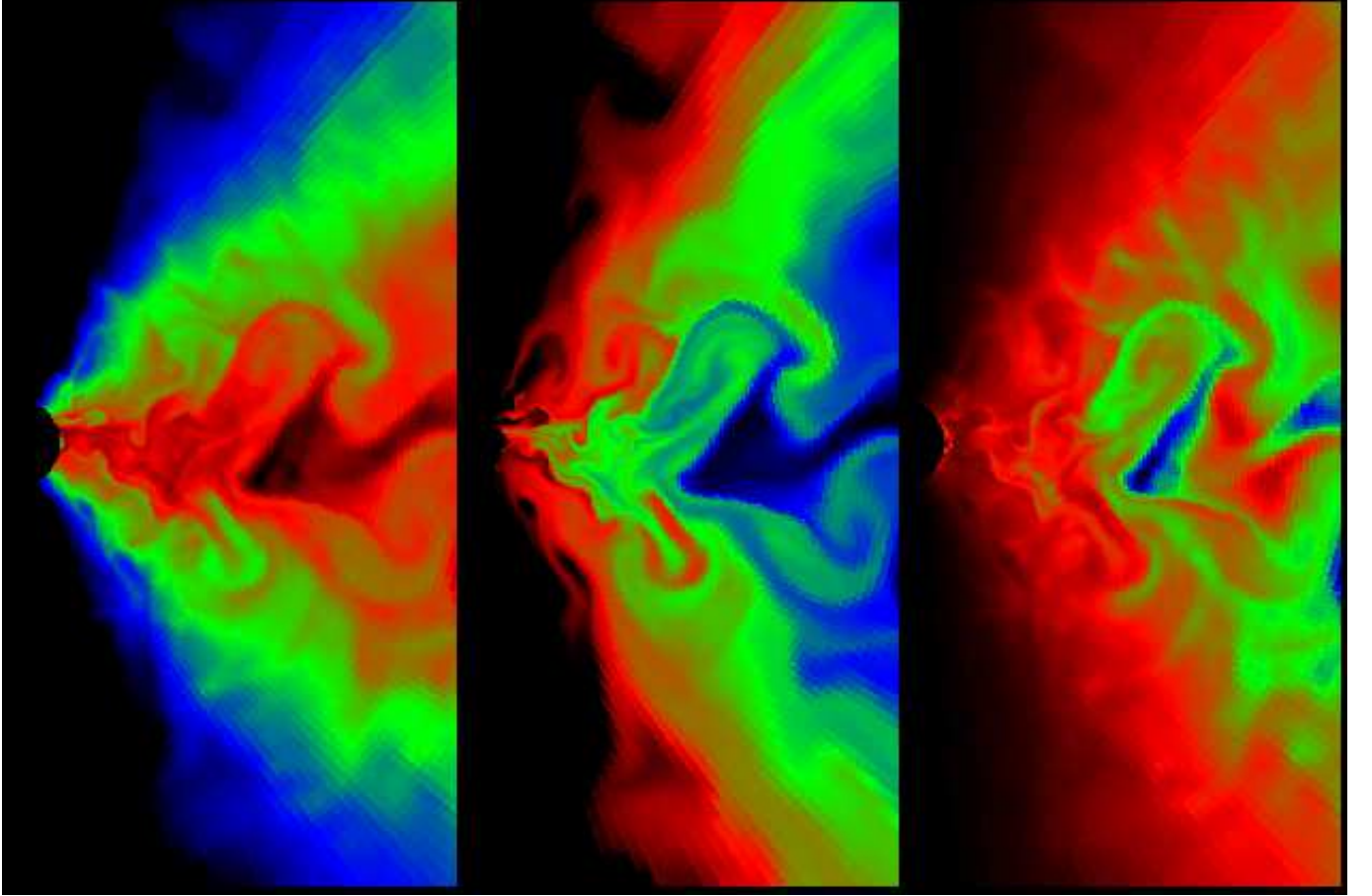


Fig. 3.— Images of the logarithm of the density (left panel), specific entropy (middle panel), and angular momentum excess compared to Keplerian rotation (right panel) at $t = 1.95$ orbits in the inner region $r < 0.1$ of Run B. The colour table runs from black to blue through red to black. Near the equatorial plane, note the correlation between regions of high (low) density, low (high) entropy, and a deficit (excess) of angular momentum.

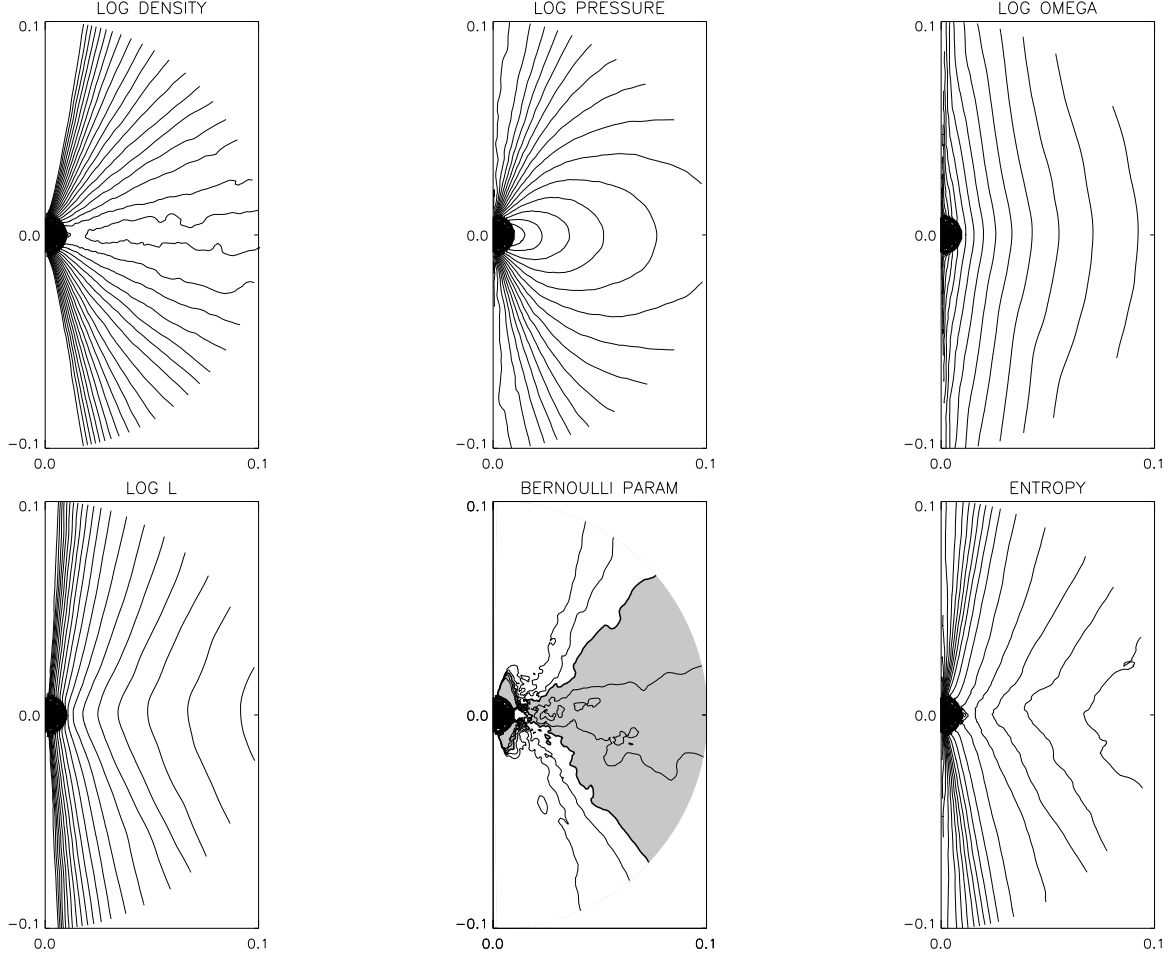


Fig. 4.— Two-dimensional structure of a variety of time-averaged quantities from the fiducial model (Run B). The minimum and maximum of $\log \rho$ are -3 and -0.69, of $\log P$ are -2.5 and 0.63, of $\log \Omega$ are 1.4 and 4.2, of $\log L$ are -2 and -0.55 and of S are 0.71 and 4.9. For these variables, twenty equally spaced contour levels are used. Only five contours between -2 and 2 are used for the plot of B (although the minimum and maximum are -29 and 1.7×10^2 respectively), with shaded regions denoting $B < 0$.

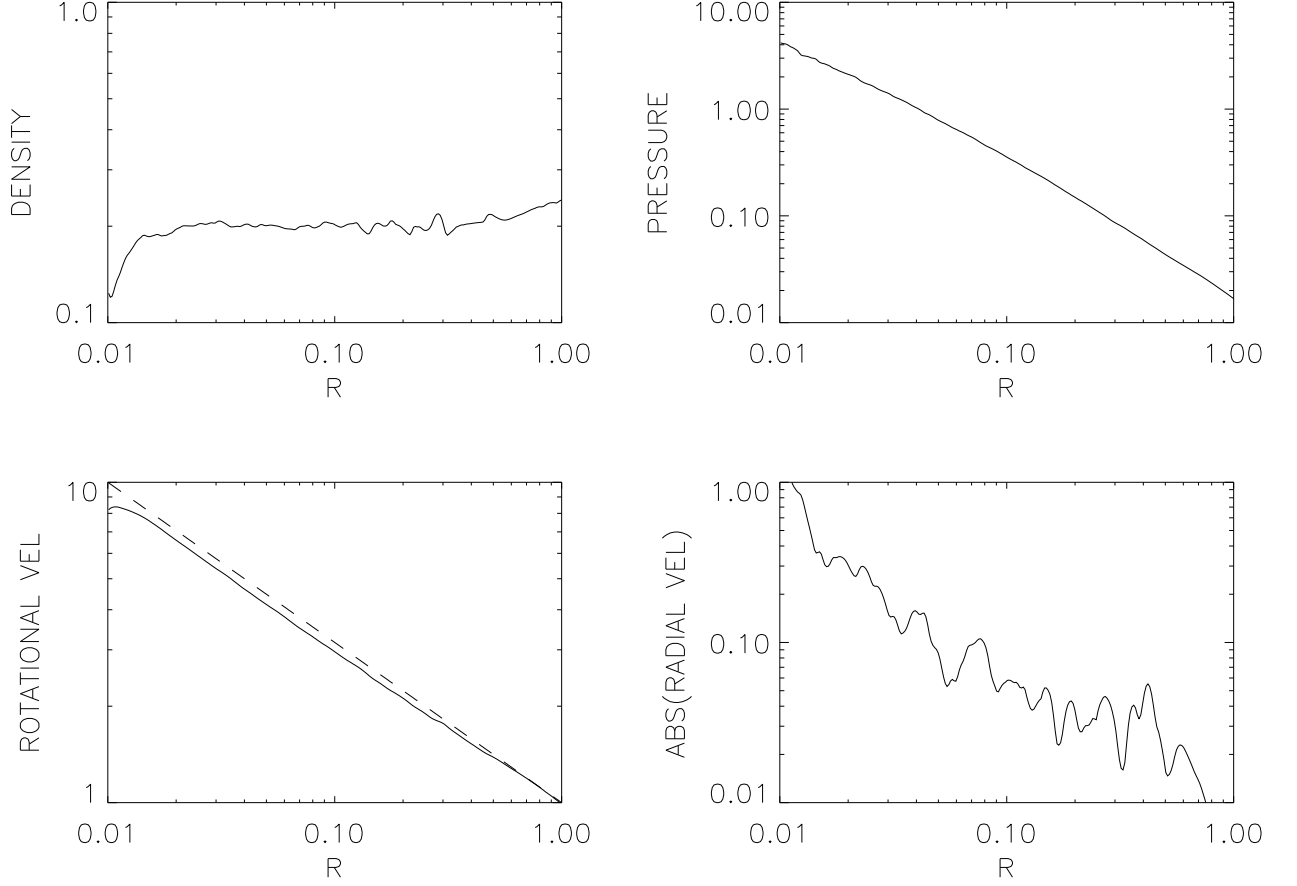


Fig. 5.— Radial scaling of some time-averaged quantities from the fiducial model (Run B). The solution is averaged over angle between $\theta = 84$ and 96 degrees to construct each plot. The dashed line in the plot of v_ϕ denotes Keplerian rotation at the equator.

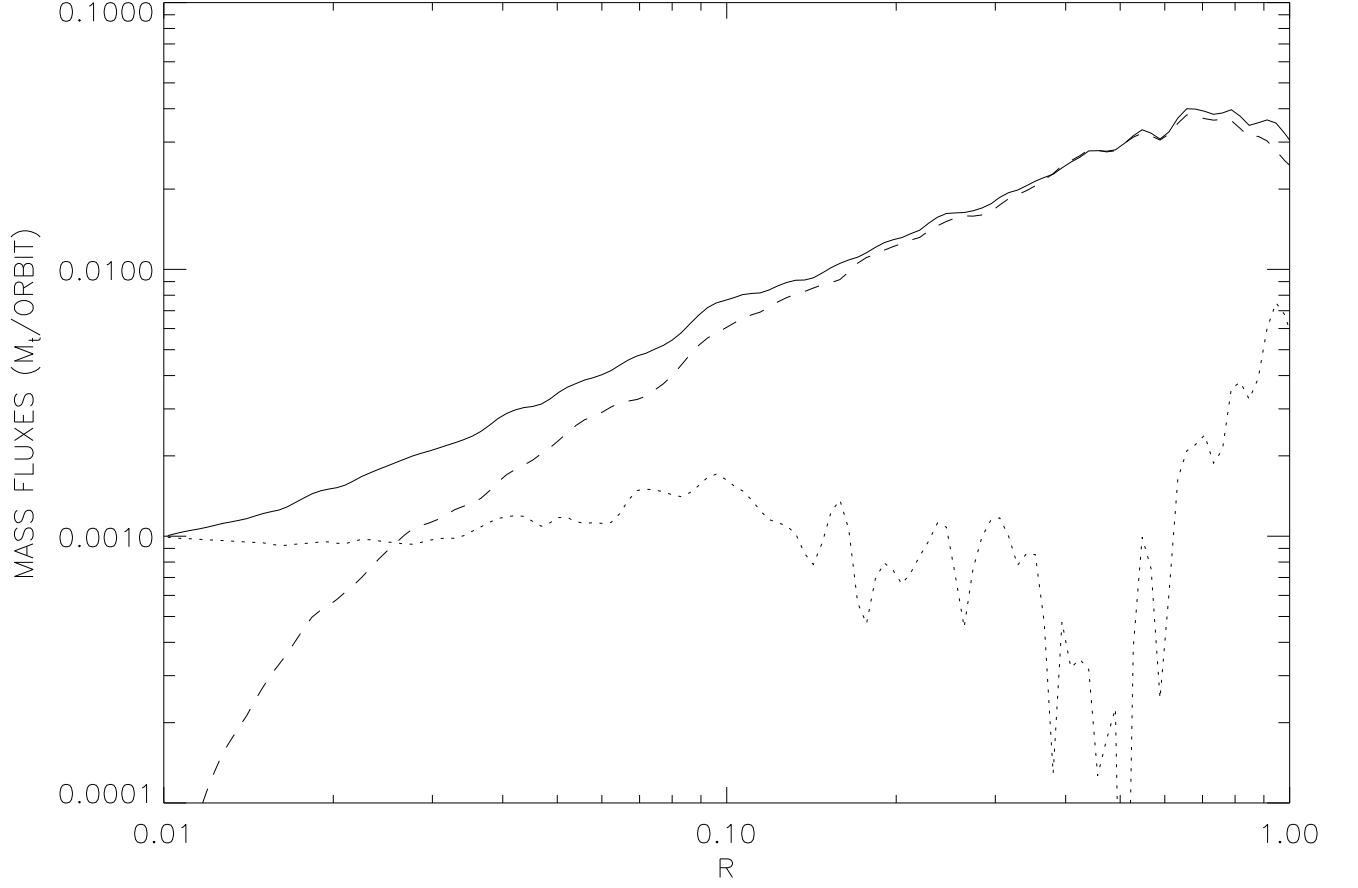


Fig. 6.— Radial scaling of the total mass inflow rate \dot{M}_{in} (solid line), total mass outflow rate \dot{M}_{out} (dashed line), and the net mass accretion rate \dot{M}_{acc} (dotted line) in the fiducial model (Run B). These fluxes are defined by equations 8, 10, and 11 in the text.

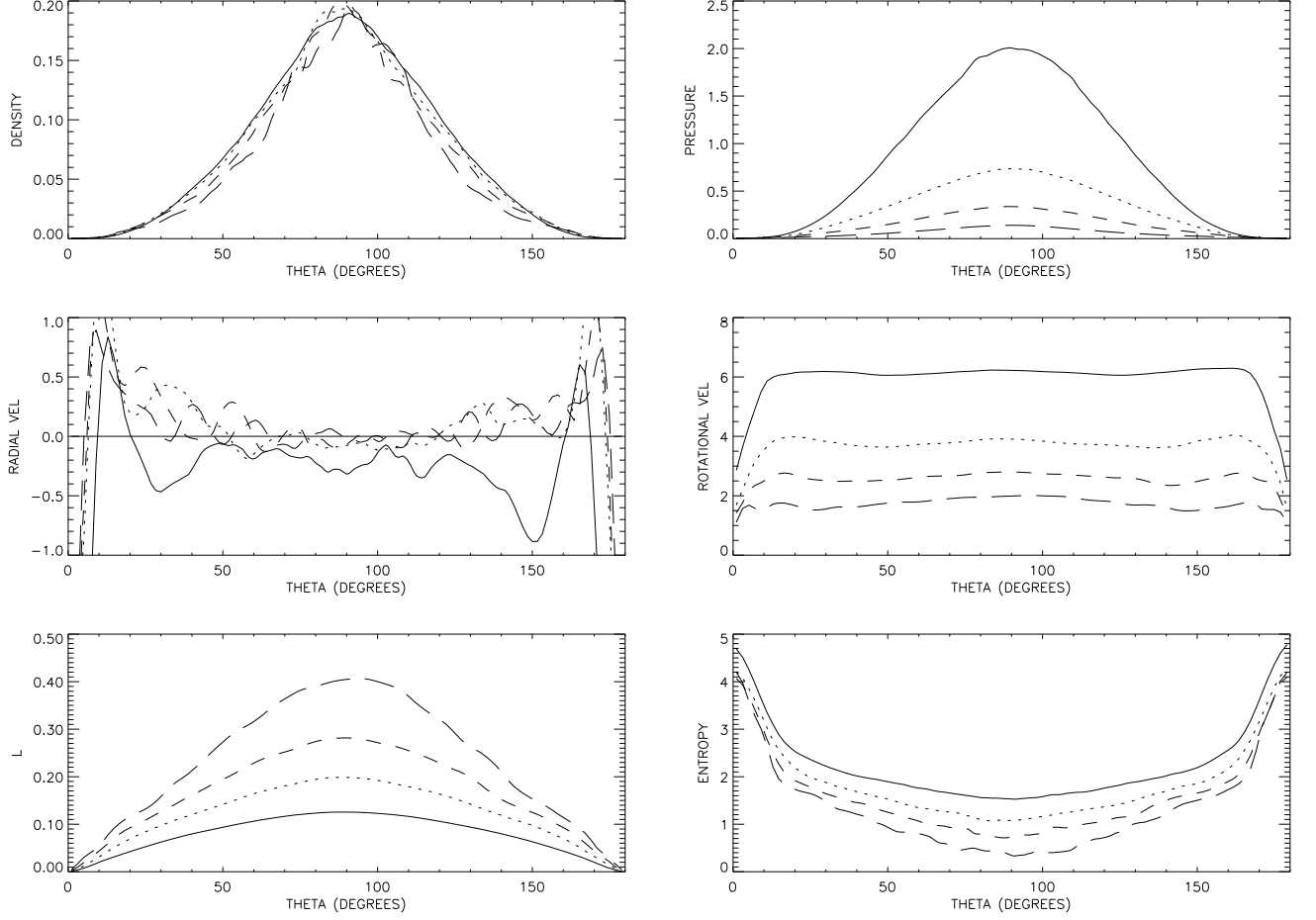


Fig. 7.— Angular profiles of a variety of time-averaged variables from the fiducial model (Run B) at radial positions of $r = 2R_B$ (solid line), $r = 5R_B$ (dotted line), $r = 10R_B$ (dashed line), and $r = 20R_B$ (long-dashed line).

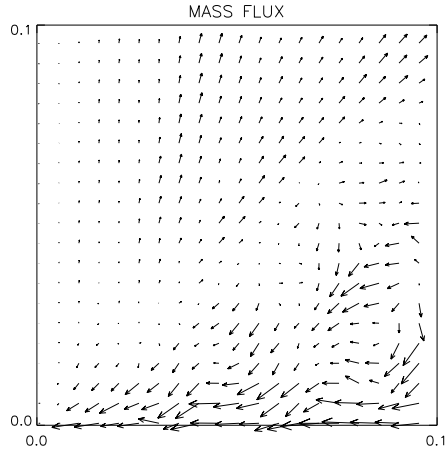


Fig. 8.— Vectors of the time-averaged mass flux in the fiducial model (Run B). The data has also been averaged across the equator and the vectors have been scaled by r . The maximum vector length corresponds to a mass flux of magnitude 0.26 (in units where $G = M = R_0 = 1$) at $r = 0.01$.

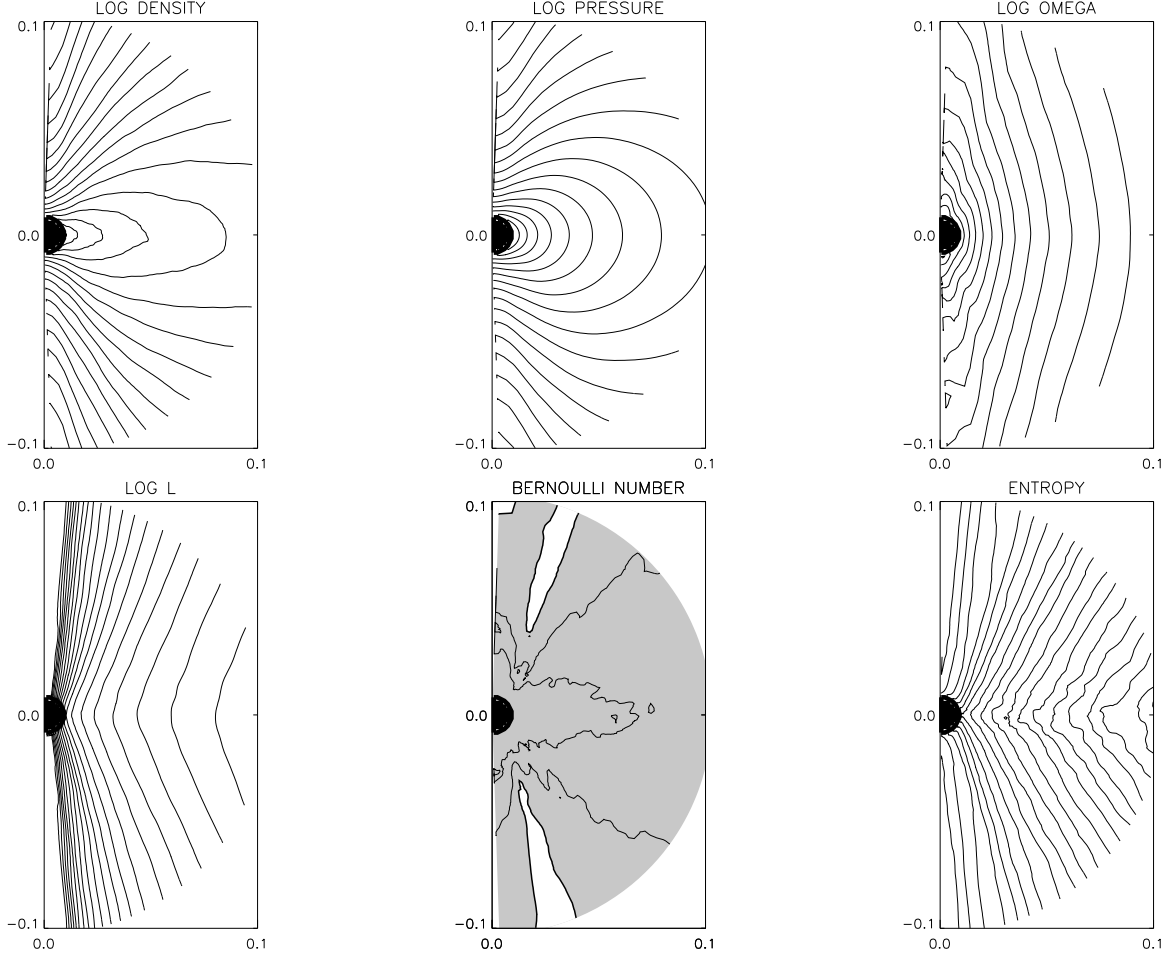


Fig. 9.— Two-dimensional structure of a variety of time-averaged quantities from the $\nu = 10^{-3}r^{1/2}$ model (Run K). The minimum and maximum of $\log \rho$ are -2.1 and 0.23, of $\log P$ are -1.5 and 1.6, of $\log \Omega$ are 1.4 and 3.0, of $\log L$ are -2 and -0.59 and of S are -0.25 and 0.29. For these variables, twenty equally spaced contour levels are used. Only three contours between -2 and 0 are used for the plot of B (although the minimum and maximum are -16 and 0.51 respectively), with shaded regions denoting $B < 0$.

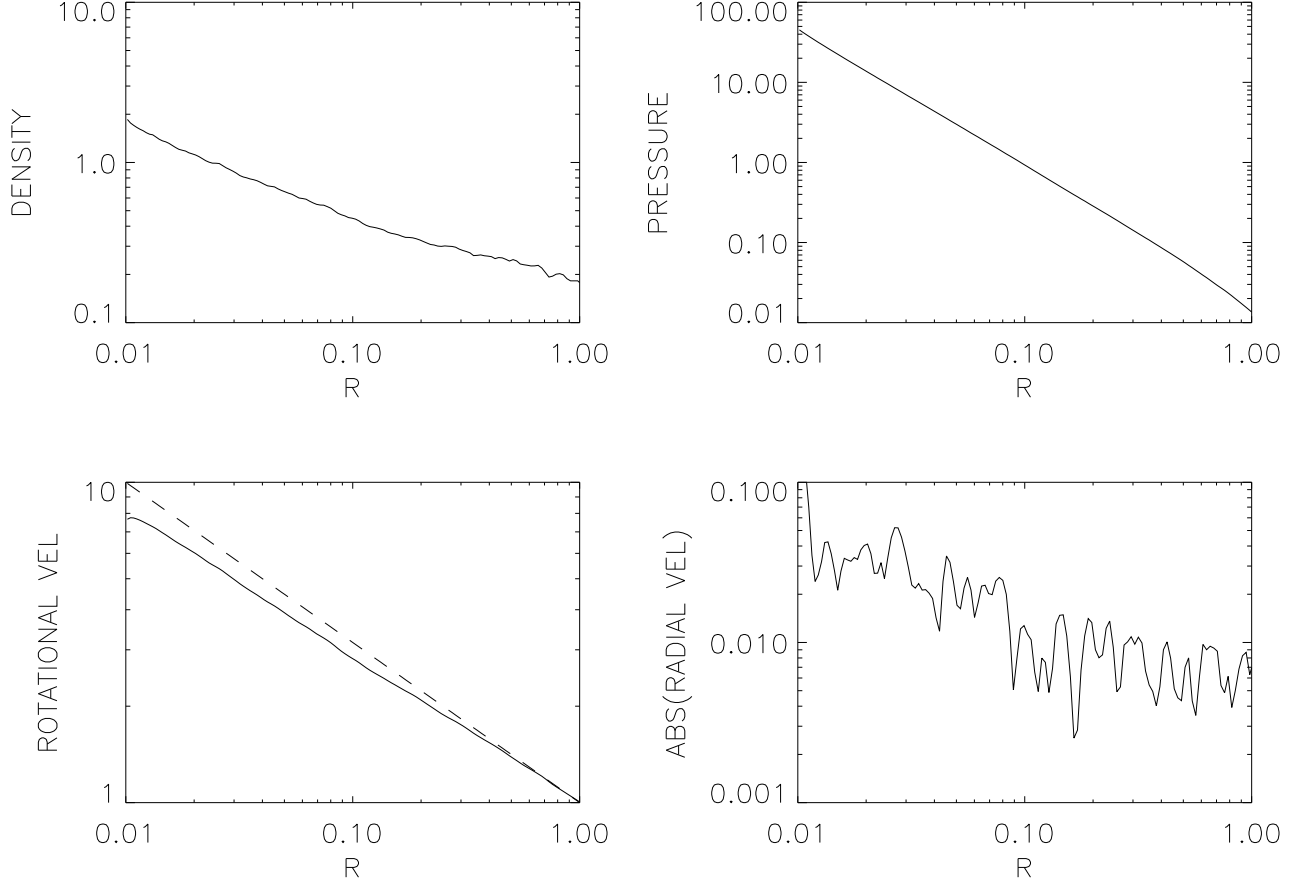


Fig. 10.— Radial scaling of some time-averaged quantities from Run K. The solution is averaged over angle between $\theta = 85$ and 95 degrees to construct each plot. The dashed line in the plot of v_ϕ denotes Keplerian rotation at the equator.

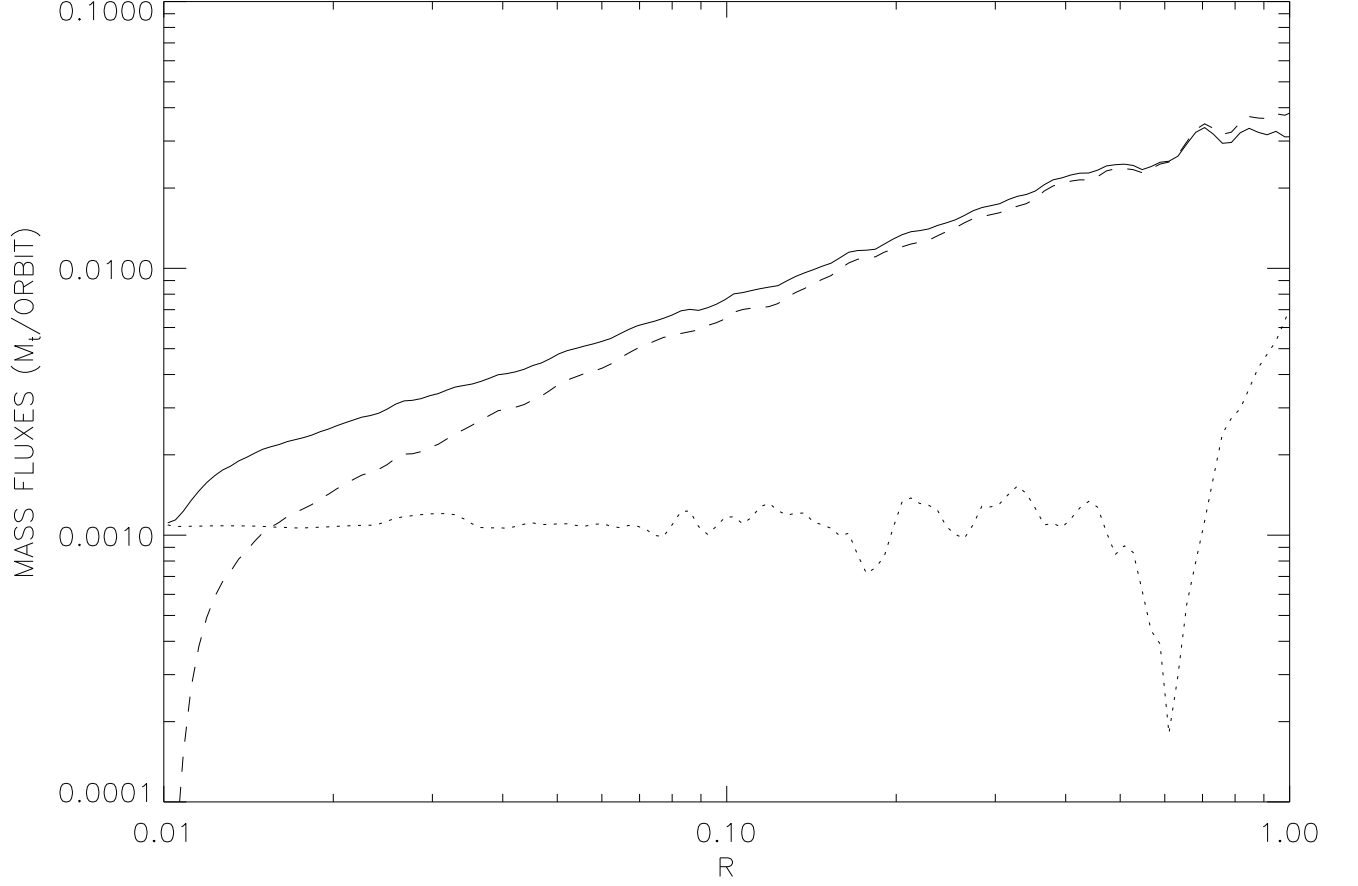


Fig. 11.— Radial scaling of the total mass inflow rate \dot{M}_{in} (solid line), total mass outflow rate \dot{M}_{out} (dashed line), and the net mass accretion rate \dot{M}_{acc} (dotted line) in Run K. These fluxes are defined by equations 8, 10, and 11 in the text.

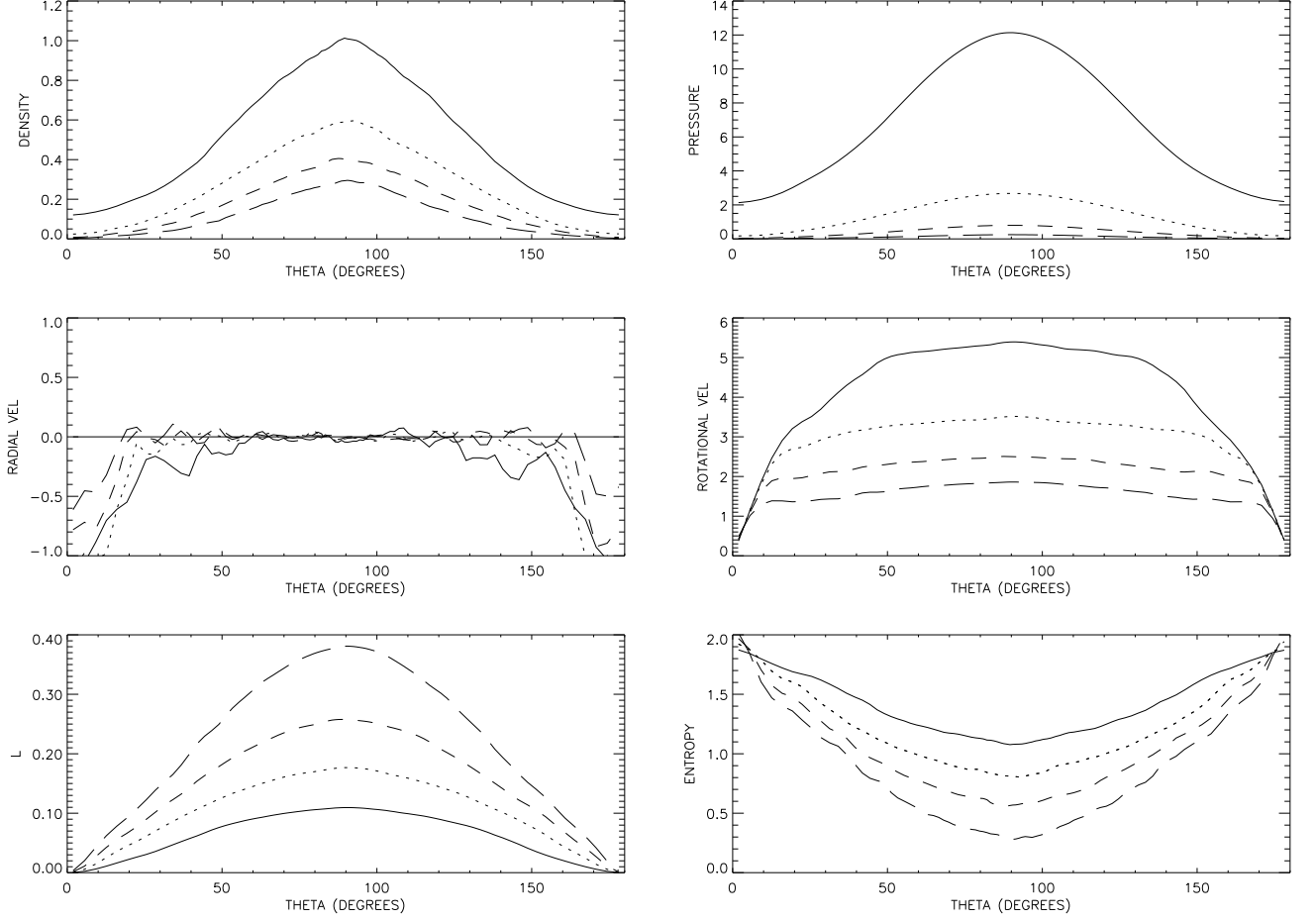


Fig. 12.— Angular profiles of a variety of time-averaged variables from Run K at radial positions of $r = 2R_B$ (solid line), $r = 5R_B$ (dotted line), $r = 10R_B$ (dashed line), and $r = 20R_B$ (long-dashed line).

REFERENCES

- Abramowicz, M.A., Chen, X., Kato, S., Lasota, J.-P., & Regev, O., 1995, ApJ, 438, L37
- Balbus, S.A., & Hawley, J.F., 1998, Rev. Mod. Phys., 70, 1.
- Begelman, M.C., & Meier, D.L., 1982, ApJ, 253, 873
- Blandford, R.D., & Begelman, M.C., 1999a, MNRAS, 303, L1.
- Blandford, R.D., & Begelman, M.C., 1999b in preparation.
- Brandenburg, A., Nordlund, A., Stein, R.F., & Torkelsson, U., 1985, ApJ, 446, 741
- Chen, X., Taam, R.E., Abramowicz, M.A., & Igumenshchev, I.V., 1997, MNRAS, 285, 439
- Gilham, S., 1981, MNRAS, 195, 755
- Hawley, J.F., Smarr, L.L., & Wilson, J.R. 1984a, ApJ 277, 296
- Hawley, J.F., Smarr, L.L., & Wilson, J.R. 1984b, ApJS 55, 211
- Hawley, J.F., 1986, in Radiation Hydrodynamics in Stars and Compact Objects, ed. by D. Mihalas & K.-H. Winkler (New York:Springer), p369
- Hawley, J.F., Gammie, C.F., & Balbus, S.A., 1995, ApJ, 440, 742
- Hawley, J.F., Gammie, C.F., & Balbus, S.A., 1996, ApJ, 464, 690
- Ichimaru, S., 1977, ApJ, 214, 840.
- Igumenshchev, I.V., Chen, X., & Abramowicz, M.A. 1996, MNRAS, 278, 236
- Igumenshchev, I.V., & Beloborodov, A.M. 1997, MNRAS, 284, 767
- Igumenshchev, I.V. 1999, preprint.
- Igumenshchev, I.V., & Abramowicz, M.A. 1999, MNRAS, 303, 309
- Mestel, L., 1999, *Stellar Magnetism*, (Oxford: Clarendon Press).
- Molteni, D., Lanzafame, G., & Chakrabarti, S., 1994, ApJ 425, 161
- Narayan, R., & Yi, I., 1994, ApJ, 428, L13
- Narayan, R., & Yi, I., 1995, ApJ, 444, 231
- Narayan, R., Mahadevan, R., Grindlay, J.E., Popham, R.G., & Gammie, C., 1998, ApJ 492, 554
- Ogilvie, G.I., 1999, MNRAS, 306, L9
- Quataert, E., & Narayan, R., 1999, submitted to ApJ

- Paczynski, B., & Wiita, J., 1980, *A&A*, 88, 23
- Papaloizou, J.C.B., & Pringle, J.E., 1984, 208, 721
- Pringle, J.E., 1981, *Ann. Rev. Astron. Astr.*, 19, 137
- Ryu, D., Brown, G.L, Ostriker, J.P., & Loeb, A., 1995, *ApJ*, 452, 364
- Stone, J.M., & Norman, M.L., 1992, *ApJS*, 80, 753
- Stone, J.M., Hawley, J.F., Gammie, C.F., & Balbus, S.A., 1996, *ApJ*, 463, 656
- Urpin, V.A., 1983, *Astr. Sp. Sci.*, 90, 79.
- Urpin, V.A., 1984, *Sov. Astron.*, 28, 50.
- Xu, G., & Chen, X., 1997, *ApJ*, 489, L29